Experimental investigation of the behaviour of a simulant material for plastic-bonded explosives and modelling of the effectivity and damage induced anisotropy

Marwen Chatti, Michel Gratton, Michael Caliez, Arnaud Frachon, Didier Picart, Nourredine Aït Hocine

Version of Record: https://www.sciencedirect.com/science/article/pii/S0167663622001594
Manuscript_4675a98ac94ea73afd364da1947af09d

Experimental investigation of the behaviour of a simulant material for Plastic-Bonded Explosives and modelling of the effectivity and damage induced anisotropy

Marwen Chatti[1*], Michel Gratton[1], Michael Caliez[1], Arnaud Frachon[1], Didier Picart[2], Nourredine Aït Hocine[1]

[1] INSA CVL, Univ. Tours, Univ. Orléans, LaMé, 3 rue de la Chocolaterie, 41000 Blois, France
[2] CEA DAM Le Ripault, F-37260 Monts, France

*Corresponding author: chatti.marwen@hotmail.fr

Abstract. This paper presents an original experimental investigation and modelling of the behaviour of a simulant material for Plastic-Bonded Explosives (PBXs). The conducted tests are tension, compression, alternated tension/compression, confined compression, channel-die, and DMA. The experimental dispositive and protocols are presented and detailed. Monotonic and cyclic tests are conducted in addition to alternated and non-proportional tests. The obtained results are presented and discussed. A special focus was put on the damage induced anisotropy and the effectivity in the material behaviour. Also, hydrostatic pressure and strain rate dependencies and the presence of hysteresis loops and irreversible strains, are highlighted.

Based on the experimental results, damage evolution laws and novel effectivity functions are proposed to model the material behaviour in the quasi-static domain.

Keywords: plastic-bonded explosives, simulant, experiments, damage induced anisotropy, effectivity, viscoelasticity, plasticity

1. Introduction

Plastic-Boded Explosives (PBXs) used for pyrotechnic structures are commonly subjected to quasi-static loadings during storage and transportation which can induce high stress levels affecting the material behaviour. These stress levels can generate the ignition of the explosive due to a local hot spot released by friction and/or the reactive decomposition (combustion or

deflagration) influenced by the permeation of hot gas into the damaged material and the microcracks network (Picart & Pompon, 2016) (You, et al., 2015). The PBX material is an HMX (octahydro-1,3,5,7-tetranitro-1,3,5,7-tetrazocine) based energetic material. Its microstructure is composed of more than 95wt% of energetic crystals mixed with a low percentage of a polymer binder. The mixture is pressed using an isostatic compaction process, which reduces the void of the material but induces inter- and intra-granular microcracks due to the high volume fraction of the solid phase (Le, et al., 2010) (Picart, et al., 2014).

Many experimental works were published about different types of PBX materials (PBX9501, PBX9502, EDC37 or LX-14) submitted to quasi-static loadings (Plassart, et al., 2020) (Belmas, 1994) (Idar, et al., 1998) (Wiegand, 2000) (Ellis, et al., 2005) (Williamson, et al., 2008) (Le, et al., 2010) (Picart, et al., 2014). The energetic material presents a nonlinear behaviour, whatever the loading conditions, with an asymmetry between tension and compression. Tension tests show a quasi-linear and quasi-brittle behaviour, unlike compression and triaxial tests that display more ductile and nonlinear behaviour (Rja Fi Allah, 2006) (Le, 2007) (Ellis, et al., 2005) (Benelfellah, 2013). Strain rate, temperature and hydrostatic pressure dependencies were also observed (Le, et al., 2010) (Caliez, et al., 2014). Aggregate materials show commonly, a hydrostatic pressure dependency because of its quasi-compact microstructure. For PBXs, the initial stiffness strongly depends on the hydrostatic pressure which shows the effect of the damaged initial microstructure. Picart et al. (Picart, et al., 2012) analysed the evolution of the microstructure of a PBX during an instrumented reverse edge-on impact test. New microcracks and shear bands in the grains were observed in addition to debonding. Ravindran et al. (Ravindran, et al., 2016) performed dynamic compression tests on a polymer bonded sugar (a known simulate for PBXs). It was observed that the local strain distribution is highly heterogeneous with large strain localization occurring between the crystal boundaries. The microstructure shows crushed crystals areas. Most of the crystals deformations are minimal, and usually realign themselves with large deformation of the binder by rigid rotation and sliding. Using also dynamic compression, Parab et al. (Parab, et al., 2016) observed that most of the cracking in the crystals was due to the tensile stress generated by the diametral compression applied from the contacts between the crystals. Tensile stress driven cracking was also observed for some of the crystals due to the transverse deformation of the binder and superior bonding between the crystal and the binder. Trumel et al. (Trumel, et al., 2010), in a Hopkinson test, observed a preferred

orientation for microcracks. They showed a common normal to the direction of extension. Picart et al. (Picart, et al., 2014) presented a uniaxial tension test followed by compression test. The damage generated in tension doesn't seem to affect the behaviour of the material in compression. Also, the material stiffness is progressively recovered. The opposite test was performed also. The prior loading in compression, seems to affect the behaviour in tension and to yield a brittle failure. Recently, Benelfellah et al. (Benelfellah, et al., 2014) (Picart, et al., 2014) suggested the presence of damage anisotropy induced by loading and that the material shows unilateral effect caused by the opening and the closure of microcracks. This observation is relatively recent, and these phenomena weren't studied experimentally in the literature. The published tests were only monotonic, and mostly uniaxial and proportional, and the evolution of the damage and the anisotropy weren't investigated. The mentioned conclusions, thus, need to be further studied and analysed experimentally.

To investigate these behavioural aspects, multiaxial and non-proportional tests, not existing in the literature, were developed, carried out and analysed. Also, microstructural observations were carried out to highlight, first, the initial state of the material microstructure and then the different damage and failure mechanisms.

As mentioned above, the presence of irreversible strains was highlighted at the end of recovery in cyclic tests (loading, relaxation, unloading and recovery) (Picart, et al., 2014) (Le, et al., 2010). Hysteresis loops were also observed in these tests. In the literature, this phenomenon is attributed to cracks opening in unloading along with a dissipative friction between microcracks lips in addition to viscoelasticity of the material. Unfortunately, these behavioural aspects, irreversible strains, and viscoelasticity, were rarely mentioned or analysed in the literature. Additionally, most published constitutive laws neglect these phenomena. In the present work, plasticity and viscoelasticity were studied and analysed in uniaxial, multiaxial, and non-proportional tests in addition to the DMA test.

Due to costs and security constrains, it would be very complicated and difficult to first, access the PBX material and to carry new experimental protocols directly. Following the CEA (French Atomic Energy Commission) recommendation, a simulant material, presenting the same behavioural aspects as the PBX, is used in this experimental campaign.

To model the behaviour of such complex material, a constitutive law considering all this physical phenomenon needs to be developed and identified based on this experimental investigation. Many models were developed in the last two decades for PBX materials, especially for dynamic and high-pressure loading conditions leading to ignition. The most

popular model is ViscoScram (viscoelastic statistical crack mechanics) (Bennett, et al., 1998). This model is a combination of the fragmentation theory proposed by Dienes in the early 80s for brittle materials (Dienes, 1982) (Dienes, 1996) (SCRAM) and viscoelastic Maxwell model (Visco). The SCRAM approach consists of an isotropic model with the damage related to the mean crack radius, in which the growth rate is limited to a maximum value. An update was proposed afterward by Hackett & Bennett (Hackett & Bennett, 2000). They modified the crack growth law to consider the influence of the hydrostatic pressure on the damage and on the tensile and compressive responses. Recently, Xiao et al. (Xiao, et al., 2017) described the dynamic mechanical behaviour of PBX1314 as a function of aspect ratio and inclusion concentration. They modelled the viscoelastic behaviour of the polymer binder using a generalized Maxwell model, with a Prony series representation for the stress relaxation functions. Another damage constitutive model with viscoelastic response and statistical fracture was developed by Xiao et al. (Xiao, et al., 2017) to model low velocity impact experiment, for PBX. This model is based on SCRAM approach of Dienes et al. (Dienes, et al., 2006) with a generalized Maxwell scheme. An isotropic constitutive relation is employed to describe the damage response of the material.

For quasi-static loadings, Gratton et al. (Gratton, et al., 2009) developed an isotropic model assuming the material as damageable elastic viscoplastic. An additional isotropic model that accounts for damageable viscoelasticity and plasticity was proposed by Le et al. (Le, et al., 2010) and Caliez et al. (Caliez, et al., 2014). The viscoelasticity was modelled using a generalized Maxwell chain model. Recently, Liu et al. (Liu, et al., 2020) presented a mechanical constitutive model, for PBX, that combines a porosity model and a viscoelastic–viscoplastic damage model with consideration of pressure and strain rate dependencies. The model is calibrated and tested only in compressive loading modes, specifically under hydrostatic cyclic compression, uniaxial compression at various strain rates, and triaxial compression with hydrostatic confining pressure.

As mentioned above, the most recent observation suggests that the material presents an evolving damage with induced anisotropy. Some approaches have been developed in the literature to model such damage (Maire & Chaboche, 1997) (Zhu, et al., 2008) (Bargellini, et al., 2008) (Murakami & Kamiya, 1997).

Benelfellah et al. (Benelfellah, et al., 2014) and Picart et al. (Picart, et al., 2014) proposed an elastoplastic model with damage induced anisotropy and effectivity. The authors illustrated the effect of the damage on engineering parameters and compared existing models based on

the different aspects of the material behaviour. This investigation revealed that, among the constitutive laws proposed to model the anisotropic damage induced by the loading and satisfying the thermodynamic requirements, the Microplane approach, initially developed for concrete by Bazant and Gambarova (Bazant & Gambarova, 1984), provides a powerful framework to implement complex laws. Particularly, the introduction of a unilateral effect is possible keeping a non-dissipative free energy, a continuous stress–strain response or a symmetrical stiffness tensor (Benelfellah, et al., 2014).

The proposed model is the first to introduce damage induced anisotropy and effectivity functions. The damage evolution laws were rather simple, and the effectivity functions were defined using Heaviside functions. The latter functions are unable to model the gradual stiffening of the behaviour and the nonlinearity of the unloading (Hysteresis loops). Also, the proposed model didn't account for viscoelasticity.

Based on the experimental results and the analysis of the damage and effectivity, new damage evolution laws and effectivity functions are proposed. In addition, viscoelasticity and plasticity will be analysed using relaxation and recovery steps in tension and compression, in addition to DMA test to characterize, in the future, a viscoelastic plastic constitutive law with effectivity and damage induced anisotropy.

2. Experiments

2.1 Material

The simulant material is an aggregate composite constituted of inert crystals and polymeric binder. The crystals are composed of 29.3wt% of barium meal (BaSO4) and 65.2wt% of melamine. The crystals size ranges from 1 to 100 µm (Bailly, et al., 2011). The binder is of small amount, 5.5wt%. It is made of an epoxy resin and a blue pigment. The material is manufactured by hot hydrostatic press moulding. The manufacturing process induces an initial damage in the simulant, like in PBXs. The resulting material has a mean density of 1.73 with a high residual porosity of 28% (Bailly, et al., 2011). The morphology and the mechanical properties of this simulant are similar to those of a PBX and both materials show the same behavioural aspects (Le, et al., 2010) (Picart & Brigolle, 2010) (Bailly, et al., 2011) (Caliez, et al., 2014) (Liu, et al., 2009) (Yeom, et al., 2012) (Zhou, et al., 2011) (Park, et al., 2013).

2.2 Test protocols and strain acquisition techniques

Microstructure observations were carried out on the pristine material and on the failure surfaces for each test using a scanning electron microscope.

Monotonic and cyclic tests were conducted, at an imposed strain rate of 2×10^{-5}/s, using a tension-compression electromechanical MTS machine. These tests consist of tension, compression, alternated tension-compression, channel-die and triaxial compression.

In tension and alternated tension/compression, strains were measured with general-purpose 90° tee rosettes, glued in the middle of the specimen, on opposite sides (two longitudinal gauges L_1 and L_2 and two transversal gauges T_1 and T_2). In compression and triaxial compression tests, three general-purpose 90° tee rosettes, glued in the middle of the specimen and spaced by 120°, were used. One longitudinal gauge was connected directly to the MTS machine to drive the test.

In cyclic tests, each cycle contains 4 steps: loading, relaxation, unloading until zero force and, finally, recovery by maintaining the zero force value. The 3 first steps are driven by the strain measured by the gauge L_1, while the last step is controlled by the load cell signal.

Previous studies (Le, et al., 2010) (Caliez, et al., 2014) showed that experimental stress-strain $(\sigma-\varepsilon)$ curves of cyclic tests are embedded below the corresponding $\sigma-\varepsilon$ experimental curves of monotonic tests, and that both tests present almost the same failure points, as observed in concrete materials (Burlion, 2010).

The test protocol and strain acquisition for the channel-die test are detailed in the correspondent section.

2.3 Uniaxial tension and compression

Dog-bone shaped specimens were used for uniaxial tension tests, with a cross-section of 9x10 mm² and a total length of 150 mm. A specific gripping fixture was designed, to ensure the homogeneous loading during the test (Figure 1). It is worth noting that tension tests are delicate to achieve because of the quasi-brittle behaviour of the studied material.

In compression, cylindrical samples of 10 mm diameter and 20 mm height were used. The specimen was pressed between two compression platens through the intermediate of two hard papers of 10.4 mm diameter and 1 mm thickness to prevent misalignment and geometric defaults (Figure 2). Monotonic and cyclic tension and compression tests were conducted. Relaxation and recovery steps last 1800 sec in uniaxial experiments.

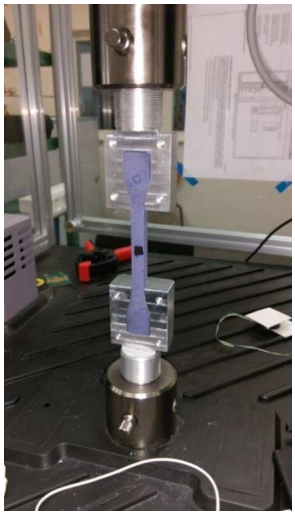

Figure 1. Tension experimental dispositive

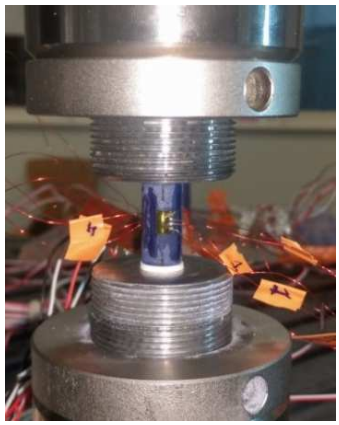

Figure 2. Compression experimental dispositive

2.4 Alternated tension-compression tests

The alternated tests: tension-compression-tension (TCT) and compression-tension-compression (CTC) were conducted using the tension experimental dispositive and dog-bone specimens. The cross-section has been adjusted to 8.5×8.5 mm² to guarantee a relatively homogeneous stress in the central zone of the specimen, while avoiding buckling in compression. The TCT test (resp. CTC), consists first, on performing few cycles in tension (resp. compression in CTC) approaching failure (80%). At the end of the recovery of the last cycle, a cyclic compression (resp. cyclic tension in CTC) is applied without reaching failure also. Finally, the specimen is again subjected to cyclic tension (resp. cyclic compression in CTC) until failure. Four general-purpose 90° tee rosettes were glued in the middle of the specimen, on opposite sides to detect a possible buckling. Relaxation and recovery steps last 1800 sec in uniaxial experiments.

2.5 Triaxial compression

Cyclic triaxial compression tests were performed using compression specimens, at hydrostatic pressure levels of 5 MPa and 10 MPa. Figure 3 presents the experimental dispositive. The specimen was glued inside a pressure vessel filled with distilled water. A pressure system group and a sensor mounted on the vessel were used to control the hydrostatic pressure level. A rod compressing the specimen inside the vessel was mounted on the MTS machine to apply the longitudinal load. The specimen and the wires were coated by a silicone gel to ensure their impermeability. Three general-purpose 90° tee rosettes were glued in the middle of the specimen spaced by 120°. Relaxation and recovery steps last 1200

sec in triaxial compression.

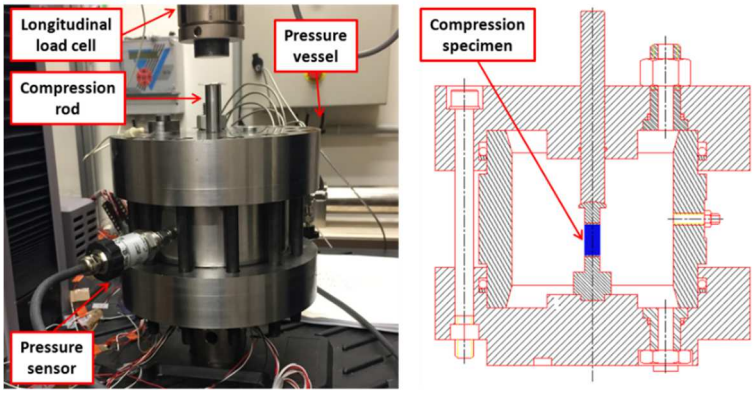

Figure 3. Triaxial compression experimental dispositive

2.6 Channel-die

Channel-die tests consist of a biaxial monotonic loading performed on cubic specimens of 15×15×15 mm^3. These experiments enable obtaining several biaxial compression points by varying the ratio between transversal and longitudinal loadings, using a specific experimental setup. Figure 4 presents the designed experimental dispositive and test details. The specimen is loaded in the longitudinal direction, using the MTS machine, and in the transversal direction T_1, using an additional load cell, while the transversal direction T_2 is left free. Two strain gauges were glued on the two opposite free sides of the cube to measure the longitudinal strain ε_L and the transversal strain ε_{T1}. The second transversal strain ε_{T2}, in the free direction T_2, was measured using two opposite LVDT. All the specimen-setup interfaces were lubricated using a teflon-grease-teflon hard paper sandwich to avoid friction and conical fracture (Picart & Pompon, 2016), and to limit the geometric default effects.

Five monotonic channel-die tests were performed. One test consisted of applying an initial transversal loading ($\sigma_{T-initial}$ = 1 MPa), then left free during the test, and applying a longitudinal loading until failure. In two other tests, the initial transversal loading was kept constant during the test (σ_T = 2 MPa and σ_T = 10 MPa), while applying the longitudinal loading until failure. The two last tests consisted of simultaneously applying longitudinal and transversal loadings, keeping respectively a ratio of 0.5 and 1 between σ_T and σ_L until failure.

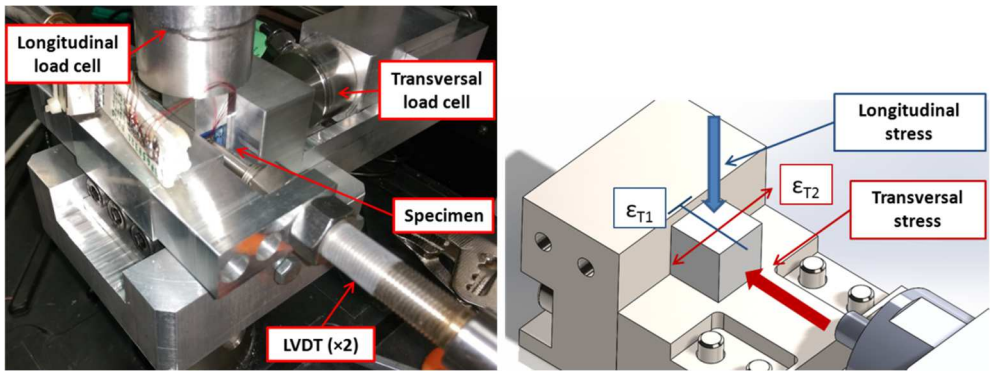

Figure 4. Channel-die experimental dispositive

2.7 Dynamic mechanical analysis DMA

Dynamic Mechanical Analysis (DMA) allows the study of the viscoelastic properties of the material as a function of the strain or the frequency, by loading the specimen under cyclic loads with very low amplitudes. This test allows to determine the storage modulus E' which characterizes the elastic part, the loss modulus E'' which characterizes the viscous part and the damping factor $tan\delta$ which characterizes the damping of the material.

The first test consists of dynamic strain sweep until a maximal value of ε_{dyn} = 3×10^{-4} at a frequency of 1 Hz and initial static strain in compression ε_{stat} = -3×10^{-4}. The second test consists of a frequency sweep between 1 and 520 Hz, with a dynamic strain of ε_{dyn} = 3×10^{-4} but without initial static load (ε_{stat} = 0). The same test is then repeated with a static load in compression of ε_{stat} = -3×10^{-4}.

A rectangular specimen of 4×4 mm^2 in section and 50 mm length is glued between 2 plates. The tests were carried out only at room temperature since the time-temperature equivalence is out of the focus of this paper. The specimen self-heating should be negligeable based on the material constituents thermal properties and the number of cycles during the DMA test.

3. Experimental characterisation of the material behaviour

Given the diversity of the conducted tests, it is necessary to adopt a common strategy for the results post-processing. Figure 5 presents the points A_i, B_i, C_i, D_i and A_{i+1} in the strain-stress plane $(\sigma - \varepsilon)$ allowing the post processing of the different behavioural aspects at each cycle:

- $[OA_1]$, when it exists, represents the hydrostatic pressurization phase.
- $[A_iB_i]$ and $[C_iD_i]$ represent, respectively, loading and unloading phases.
- $[B_iC_i]$ and $[D_iA_{i+1}]$ represent, respectively, the relaxation and recovery phases. During

post processing, these steps are linearly extended, in a Log time scale, up to 10^4 sec for a real estimation of the relaxed stress in relaxation (point C_i) and irreversible strain in recovery (point A_i, longitudinally and transversally).

- The slope of $[C_i A_{i+1}]$ describes the secant elastic modulus (damaged), noted E.
- For the unconfined tests, the final point of recovery A_{i+1} represents the residual plastic strain: $\varepsilon_p = [A_1 A_{i+1}]$. In this case, $O \equiv A_1$.
- Confined tests require a virtual hydrostatic unloading to obtain the point G_{i+1} corresponding to the residual strain. To simplify the identification process, it is assumed that the hydrostatic unloading is from the undamaged isotropic compressibility module K_0 (the slope of $[A_{i+1} G_{i+1}]$ is therefore equal to $3K_0$). With this hypothesis, a common approach to identify the current residual strain is obtained $\varepsilon_p = [O G_{i+1}] = [A_1 A_{i+1}]$.

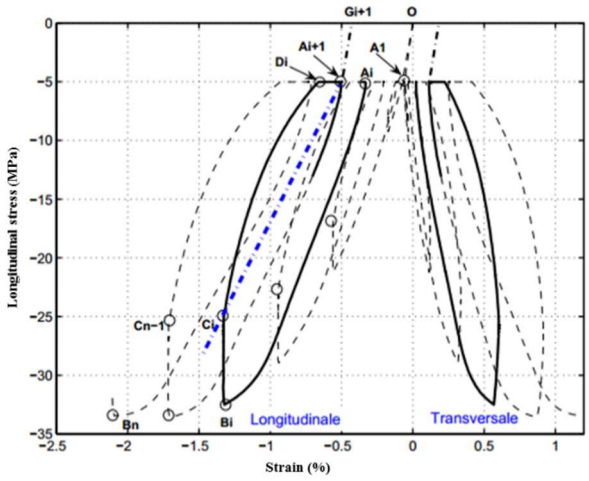

Figure 5. Characteristic points of a load-relaxation-unloading-recovery cycle for triaxial compression test (5 MPa) and strain rate of 2×10^{-5}/s

3.1 Microstructural observations of the material damage

Figure 6 show the different constituents of the pristine material. The brilliant phases correspondents probably to the Barium crystals $BaSO_4$. High solid fraction of crystals is observed in the microstructure. The binder cannot be identified clearly. The initial microstructure reveals the presence of initial microcracks generated by the manufacturing process.

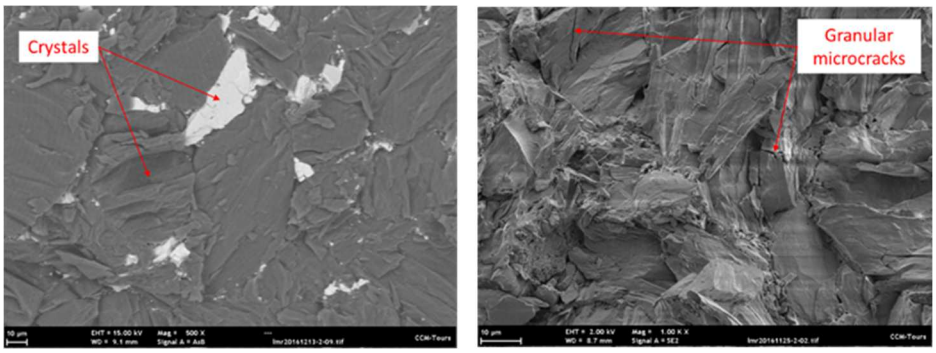

Figure 6. Microstructure of the pristine material

Figure 7 shows the microstructure of the material loaded in tension. Barium meal crystals appear to be grey. A clearer material is observed between these crystals, that may contain melamine crystals and binder. It's very hard to distinguish only the binder because of its small amount.

The observation of the failure surfaces in tension shows long microcracks developed in the interface binder-crystals and, to a lesser extent, inside the crystals. The microcracks orientations are random, and the damage seems to propagate in all directions. Despite the presence of some broken crystals, this failure mode doesn't seem dominant.

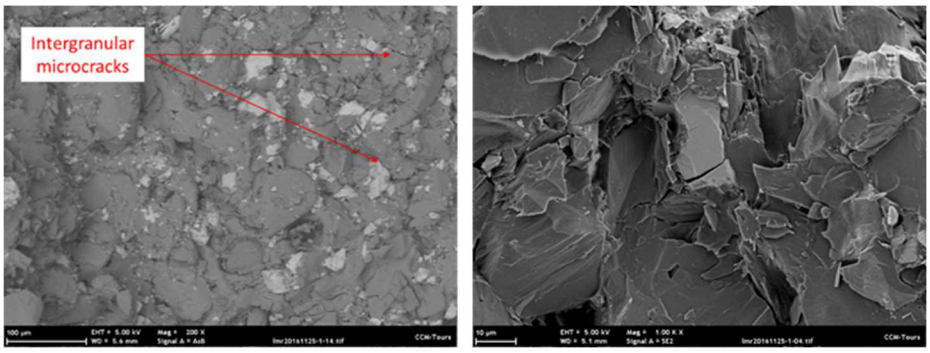

Figure 7. Microstructure of the material loaded in tension

Based on the aspect of the microstructure, failure surfaces observed in compression show clearly higher levels of damage and a different failure mode compared to tension, as observed in Figure 8. In addition to intergranular cracks, some regions in the microstructure present a high concentration of small crystals due to a violent fracture of big crystals. Some shear bands are observed also proving the presence of friction and irreversible strains. Same as tension, microcracks are randomly orientated, and the damage propagates in all directions.

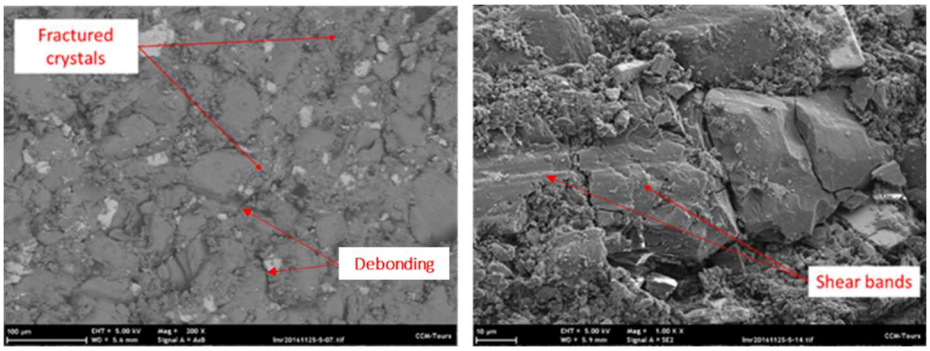

Figure 8. Microstructure of the material loaded in compression

Failure surfaces of specimens loaded under biaxial compression were also observed and analysed. The microstructure of the material is presented in Figure 9 ($\sigma_{T-initial}$ = 1 MPa) and Figure 10 ($\sigma_L = \sigma_T$). The microstructure presents the same debonding and fractured crystals, like compression but in a more concentrated manner. However, an unexpected phenomenon consisting of the presence of voids in the microstructure was observed. This phenomenon seems to be due to crystals tearing under the high stress levels in biaxial compression.

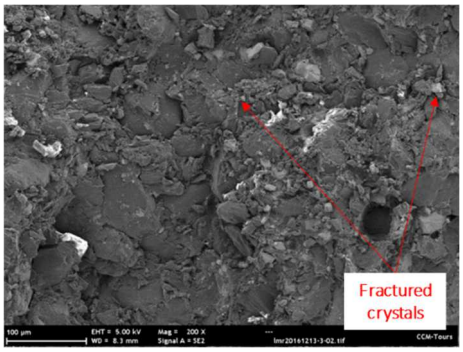

Figure 9. Microstructure of the material loaded in channel die ($\sigma_{T-initial}$ = 1 MPa)

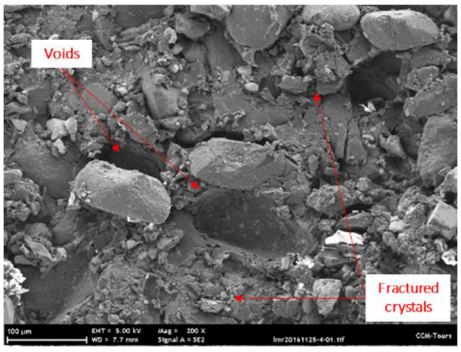

Figure 10. Microstructure of the material loaded in channel die ($\sigma_L = \sigma_T$)

3.2 Behaviour asymmetry between tension and compression

Stress-Strain ($\sigma - \varepsilon$) curves obtained from tension, compression, CTC and TCT are reported, respectively in Figure 11, Figure 12, Figure 13 and Figure 14. It's noticed, first, that the curves of monotonic tension and monotonic compression constitute the master curves (envelope curves) for the cyclic tests. It seems that unloading-loading steps don't influence the material global behaviour. In tension, a tensile strength of 2.75 MPa and longitudinal and transversal strains of 0.26% and -0.053% are obtained respectively. In compression, the material behaviour is more ductile. In fact, the material fails at -18.84 MPa of compressive strength and -1.62% and 0.97% of longitudinal and transversal strains respectively.

The material clearly presents an asymmetry of behaviour between tension and compression

which could indicate the presence of two different damage evolutions.

The tension curves present a nonlinearity related, partially, to a damage starting from the beginning of the test, at low level of stress. The failure is quasi-brittle and happens too quickly compared to the compression. The evolution of the compression curves shows mainly two phases: a quasi-linear evolution until ~60% of the compressive strength followed by a strong nonlinearity.

The study of the evolution of the stiffness and the damage in the material is necessary to understand this asymmetry in the material behaviour.

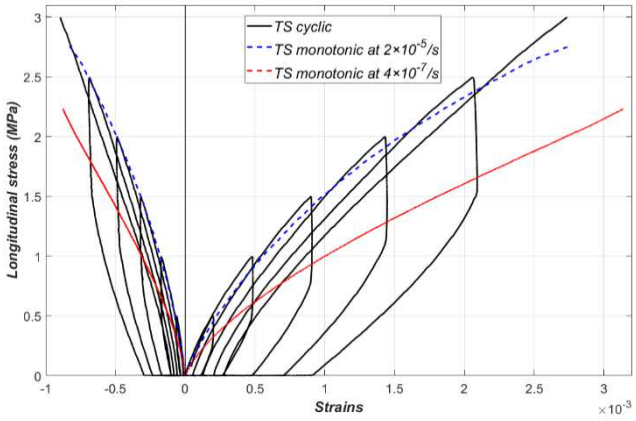

Figure 11. Monotonic and cyclic tension at $\dot{\varepsilon} = 2 \times 10^{-5} s^{-1}$ and $\dot{\varepsilon} = 4 \times 10^{-7} s^{-1}$

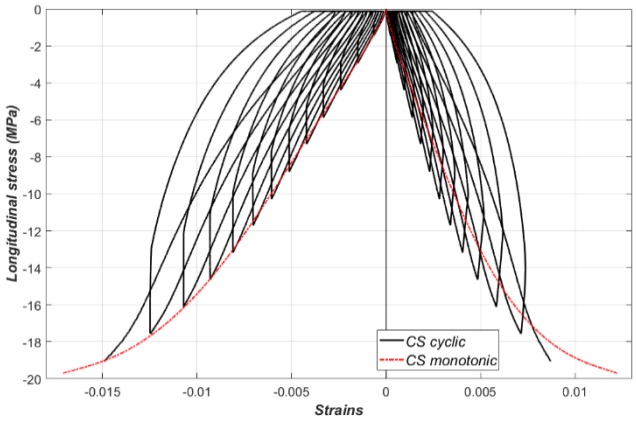

Figure 12. Monotonic and cyclic compression at $\dot{\varepsilon} = 2 \times 10^{-5} s^{-1}$

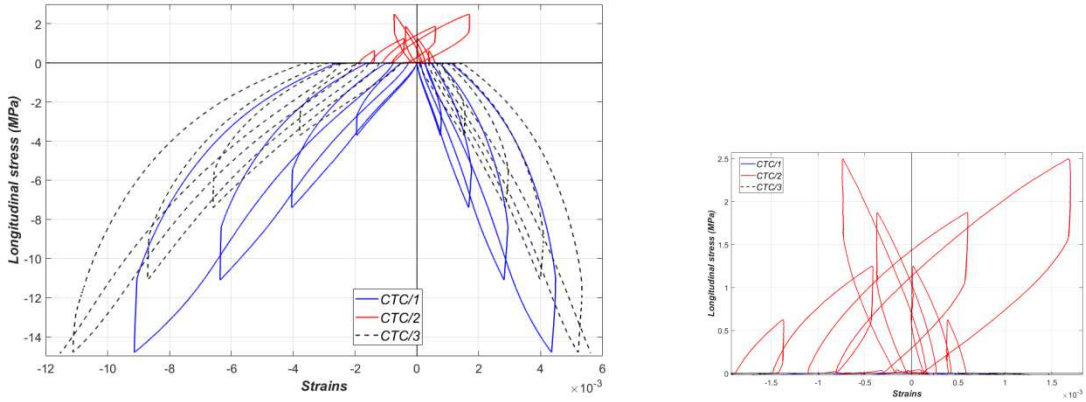

Figure 13. Cyclic Compression-Tension-Compression at $\dot{\varepsilon} = 2 \times 10^{-5} s^{-1}$

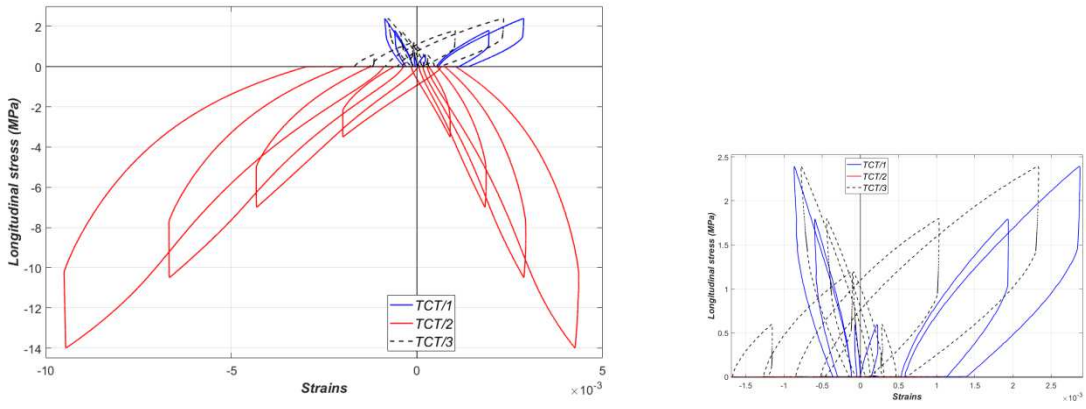

Figure 14. Cyclic Tension-Compression-Tension at $\dot{\varepsilon} = 2 \times 10^{-5} s^{-1}$

3.3 Hydrostatic pressure dependency

Stress-Strain $(\sigma - \varepsilon)$ curves obtained from triaxial compression at 5 and 10 MPa of hydrostatic pressure are shown below in Figure 15. The material response is more ductile than uniaxial compression. Two phases are observed, quasi-linear behaviour followed by a nonlinear one, same as seen in compression. At 5 MPa (resp. 10 MPa) of hydrostatic pressure, the material fails at a compressive strength of -29.8 MPa (resp. -45.9 MPa), a longitudinal strain of -2.7% (resp. -3.2%) and a transversal strain of 1.73% (resp. 1.65%). The ultimate strength and strains increase with increasing hydrostatic pressure. A type of consolidation phenomena seems to appear.

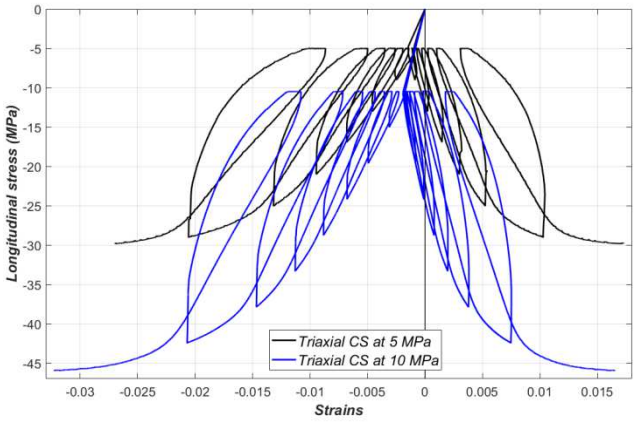

Figure 15. Cyclic triaxial compression 5 MPa and 10 MPa at $\dot{\varepsilon} = 2 \times 10^{-5} s^{-1}$

3.4 Directional damage and effectivity

3.4.1 Tension, compression and triaxial compression

Figure 16 and Figure 17 show the evolution of longitudinal and transversal secant stiffnesses as a function of the relaxed stress (stress at the end of relaxation steps and without hydrostatic pressure). The behaviour difference between tension and compression can be observed clearly.

In tension, the longitudinal stiffness decreases from the beginning of the test, when, at the same time in compression, it increases first (until 60-70% of ultimate stress) and then decreases. For triaxial compression, the latter phenomenon is more pronounced: the stiffening happens in the confinement step yielding higher initial stiffness. The stiffness decreases, then, throughout the loading.

Taking into account the initial pre-damage in the microstructure, the direct opening of the microcracks, perpendicular to the solicitation, in tension, yields a quick brittle failure. In compression and triaxial compression, the initial microcracks tend to close first inducing a linear global material behaviour and later a ductile failure with irreversible strains.

The extrapolation of the stiffness curves to zero stress allows an estimation of the initial secant stiffness E_0 for each test as seen in Table 1.

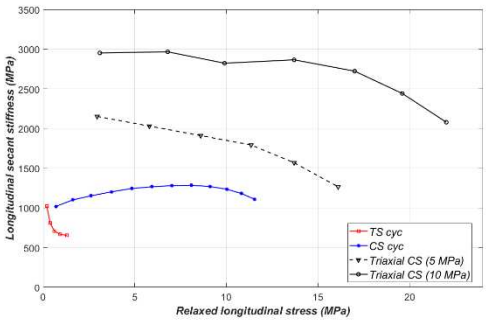

Figure 16. Evolution of the longitudinal secant stiffness in function of relaxed longitudinal stress in tension, compression and triaxial compression

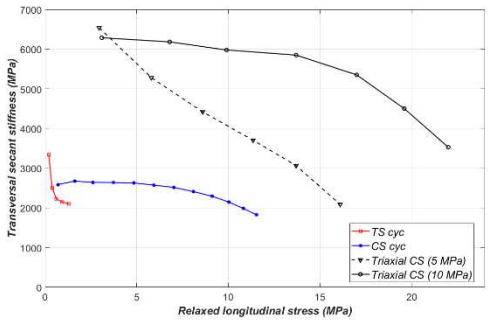

Figure 17. Evolution of the transversal secant stiffness in function of relaxed longitudinal stress in tension, compression and triaxial compression

Table 1. Initial longitudinal and transversal stiffnesses for tension, compression and triaxial compression (at 5 and 10 MPa)

Tests	E_L (MPa)	E_T (MPa)
Uniaxial tension	1000	3300
Uniaxial compression	1000	2600
Triaxial compression at 5 MPa	2150	6500
Triaxial compression at 10 MPa	3000	6300

3.4.2 Tension-compression-tension and compression-tension-compression

The alternated tests, TCT and CTC, were developed and carried out to highlight the effectivity and the suspected phenomenon of the stiffness recovery during changes of stress or strain signs. The master stress–strain $(\sigma - \varepsilon)$ curves of the cyclic CTC and TCT are compared with those of CS and TS and shown in Figure 18 and Figure 19. The longitudinal and transversal strains are initialized to zero at the start of steps 2 and 3 in TCT and CTC. The analysis of the different evolutions revealed the following observations:

- The material responses in compression and in the first step of CTC (CTC/1) are relatively the same.
- The material response in the second step of TCT (TCT/2: compression preceded by tension) presents a lower stiffness in the beginning and a higher recovery than in compression. This is interpreted by a generated damage in tension (TCT/1). The damage is visible in the beginning of the test but rapidly "deactivated" by the closing of the microcracks throughout the loading.
- The material response in the third step of TCT (TCT/3: tension preceded by tension and then compression) is quasi-linear, contrary to a simple tension. The stiffness in TCT/3 is, from the beginning of the test, is twice as low as those observed in simple tension, and

contrariwise not decreasing throughout the rest of the test. It seems that the material had been degraded in the compression step (TCT/2) even if it isn't visible in the evolution of the stiffness; effectivity seems to prevent seeing the damage in compression, although visible in tension responses in CTC/2 and TCT/3.

– These observations can be seen in the evolution of longitudinal stiffness and especially in the transversal stiffness.

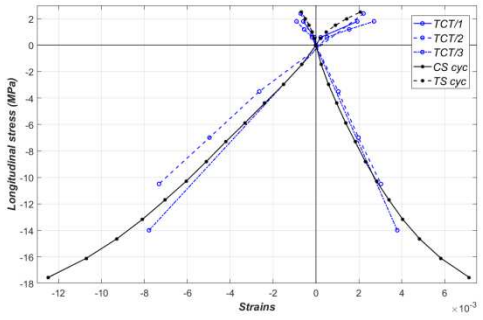

Figure 18. Master curves for cyclic TCT, CS and TS

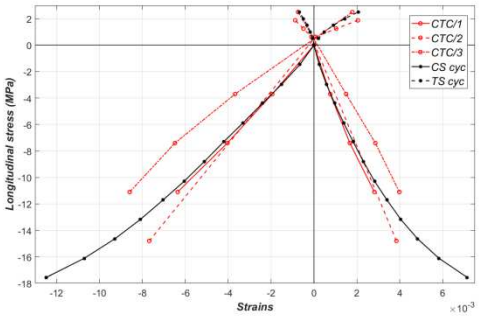

Figure 19. Master curves for cyclic CTC, CS and TS

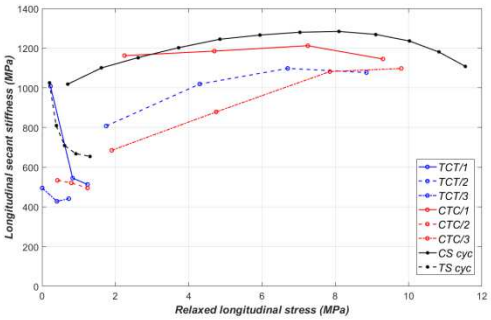

Figure 20. Evolution of the longitudinal secant stiffness in function of relaxed longitudinal stress in cyclic TCT, CTC, compression and tension

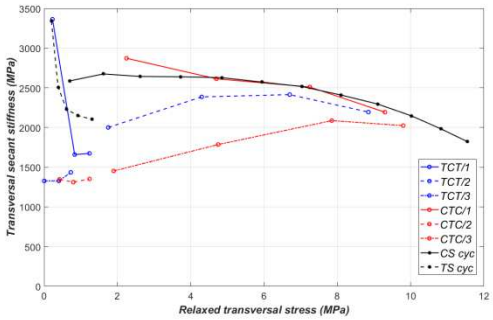

Figure 21. Evolution of the transversal secant stiffness in function of relaxed longitudinal stress in cyclic TCT, CTC, compression and tension

3.5 Contraction ratio

In the isotropic framework, the Poisson's ratio is defined from the ratio of the transversal elastic strain and the longitudinal elastic strain as, $\nu = -\varepsilon_T^e/\varepsilon_L^e$. Considering that irreversible strains don't develop during unloading and recovery, it's possible to plot the evolution of this ratio for each test (Figure 22). The obtained values are between 0.26 and 0.61. In the isotropic framework, this value shouldn't exceed 0.5. An explication of this phenomenon was advanced by Pecqueur (Pecqueur, 1995) and adopted with Dragon et al. (Bargellini, et al.,

2007) (Bargellini, et al., 2008) for brittle aggregate materials invoking induced anisotropic damage by loading.

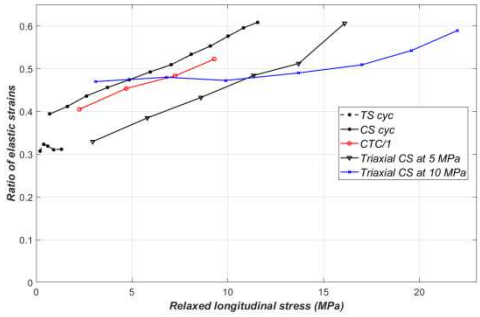

Figure 22. Evolution of the contraction ratio in tension, compression, CTC/1 and triaxial compression at 5 and 10 MPa

3.6 Strain rate dependency

The studied material presents a sensitivity to the strain rate, thus a viscoelasticity coming essentially from the polymeric binder. In cyclic tension, irreversible strains are very low and, so, the behaviour is considered mainly viscoelastic (Figure 11). Two monotonic tension tests at two different strain rates 2.10^{-5}/s and 4.10^{-7}/s were carried out. The stress-strain $(\sigma - \varepsilon)$ curves, presented in the figure above (Figure 11), clearly show a dependency of the response to the strain rates. Cyclic tests, at 2.10^{-5}/s, present relaxation and recovery steps that can be used to identify and analyse viscoelasticity. In Figure 23, the evolution of longitudinal stress in relaxation steps at low stress levels in tension and compression is shown. The curves don't seem to present a difference, meaning that there isn't an effect of the opening/closing of microcracks between tension and compression at low stress levels.

At higher stress levels, in compression, it seems that the hydrostatic pressure doesn't have much effect on the stress in relaxation (Figure 24). At the same level of stress in the beginning of relaxation, there is a very small difference between the response in compression and both responses in hydrostatic at 5 and 10 MPa. It should be noted that viscous phenomena can have viscoelastic part and a viscoplastic part because of the irreversible strains present at the end of recovery. Although ignoring this distribution during the relaxation phases, experimental results can still be analysed.

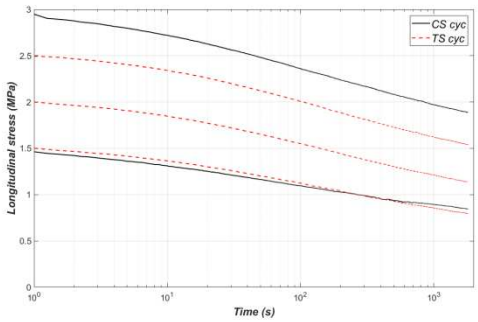

Figure 23. Evolution of σ_L in relaxation steps at low stress levels in tension and compression

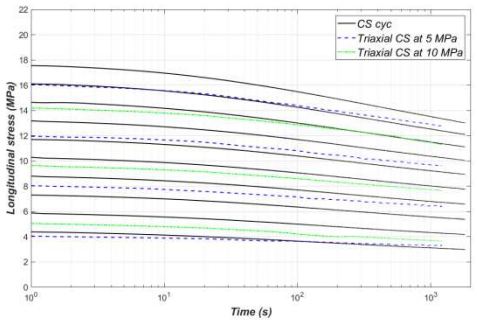

Figure 24.Evolution of σ_L in relaxation steps in compression and triaxial compression at 5 and 10 MPa – Hydrostatic pressure effect

Curves showing the evolution, in time, of the ratio between longitudinal stress in relaxation steps σ_L and the stress at the beginning of the relaxation steps σ_0, are shown in Figure 25. A nonlinearity, with respect to the stress level, is observed: curves are not superposed and with the increase of the stress level, the relaxation is slower.

Figure 26 shows the first cycle of tension, TCT/3 and CTC/2. The material response in tension on a pristine material is different from tension preceded with compression, which generates a lot of damage. In TCT/3 and CTC/2, the material relaxes more, thus reducing the relaxed stress approaching zero. The nonlinearity with respect to the stress level is more pronounced. Contrary to relaxation step, the material recovers very little yielding important irreversible strain even at low level of stress.

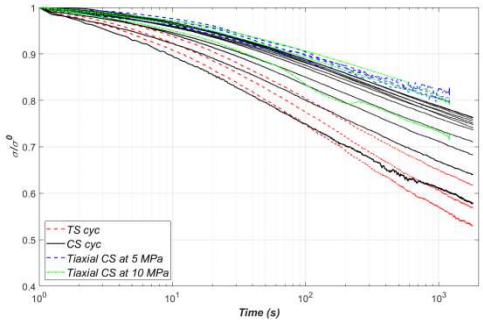

Figure 25. Evolution of the ratio of σ_L and σ_0 (stress at the beginning of relaxation) in relaxation steps in tension, compression and triaxial compression – Stress level effect

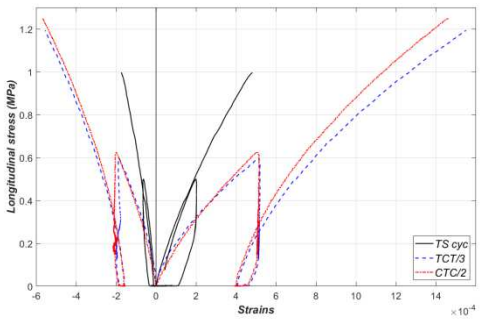

Figure 26. First step in tension and tension preceded with compression (TCT/3 and CTC/2)

In order to cover a large range of strain rates, and to better analyse the viscoelastic behaviour, DMA tests were carried out on the material. Frequency sweeps between 1 and 520 Hz at two different amplitudes of dynamic strain (ε_{dyn}), respectively 10^{-4} and 2.10^{-4}. The tests cover a range of strain rate from 6.10^{-4}/s and 6.10^{-1}/s. The first test was made without a preload and

therefore alternates tension and compression, for a maximum stress of 0.6 MPa. The second test was carried out with a static preload of -3.10^{-4}, which allows the specimen to be compressed with a stress of -2 MPa. The first step consisted in verifying the absence of nonlinearity for this level of solicitation. To do this, the specimen is loaded at a frequency of 1 Hz and a strain varying from 0 to 3×10^{-4}. A slight nonlinearity of the bulk modulus vis-à-vis the strain level appears. It decreases slightly (about 15%) while the loss modulus increases slightly (Figure 27). No clear nonlinearity appears during the increasing sweep, relatively linear, and moreover, no irreversibility appears during the decreasing sweep which is superimposed on the increasing sweep and joins the starting point of the pristine material. The second step consists on performing frequency sweep. The dependency of the storage modulus and the loss modulus is important, since for the swept range, the variation is around 60 to 70% (Figure 28). Finally, the tangent modulus at the origin of the two tensile tests (4.10^{-7}/s and 2.10^{-5}/s) and the compression test (2.10^{-5}/s) are reported on the curves describing the dynamic modules (Figure 29). It can be noted that in all tests, the failure stress increases with increasing strain rate, as expected.

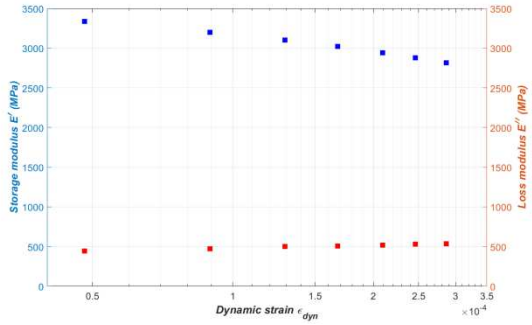

Figure 27. Evolution of E' and E" in function of ε_{dyn} in DMA test with an amplitude sweep, $\varepsilon_{stat} = -3\times10^{-4}$ and f = 1 Hz

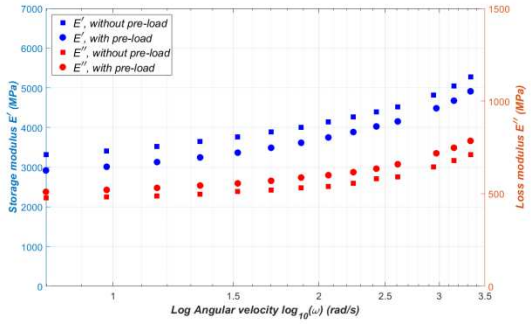

Figure 28. Evolution of E' and E" in function of ω in DMA test with a frequency sweep without preload ($\varepsilon_{stat} = 0$ et $\varepsilon_{dyn} = 10^{-4}$) and with preload ($3\times10^{-4}$ et $\varepsilon_{dyn} = 2\times10^{-4}$)

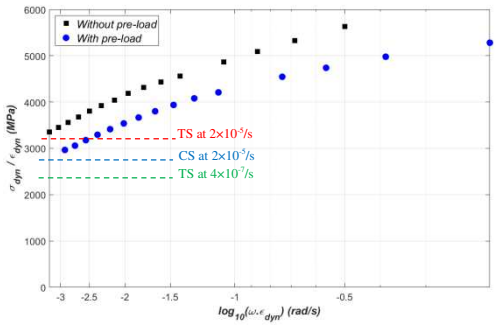

Figure 29. Evolution of the ratio (σ_{dyn} / ε_{dyn}) in function of ($\omega\times\varepsilon_{dyn}$) in DMA test with a frequency sweep without preload ($\varepsilon_{stat} = 0$ and $\varepsilon_{dyn} = 10^{-4}$) and with preload ($\varepsilon_{stat} = -3\times10^{-4}$ and $\varepsilon_{dyn} = 2\times10^{-4}$)

3.7 Biaxial strength

The developed experimental dispositive, called "Channel-die", allow to level up the absence of biaxial test machine. Those tests are mainly carried out to calibrate a failure criterion based on stress plane responses and to study the behaviour under biaxial loading. An example of a channel die test with σ_T/σ_L = 0.5, is presented in Figure 30. The evolution of the longitudinal stress is plotted in function of the 3 measured strains. The transversal strain is close to the longitudinal strain observed in triaxial compression at 10 MPa, for a level of pressure, in terms of $Tr(\underline{\underline{\sigma}})$, slightly inferior. Table 2 presents the ultimate stresses and strains at break for all carried channel die tests corresponding to the following biaxiality levels, σ_T/σ_L = {0.083; 0.17; 0.34; 0.48; 0.92}. The tests are monotonic, so the measured stresses contain a viscous part.

It can be noted, the high level of positive transversal strain associated to the free transversal direction translating thus, the dilatant character of the material.

The material strength under biaxial loading is clearly higher than under uniaxial compression: in fact, the strength increases with increasing biaxiality ratio, reaching 70% growth in the equibiaxial compression $\sigma_T/\sigma_L \approx 1$. To highlight this phenomenon, the failure stresses of compression test and channel die tests are plotted in the plane $(\sigma_1/|\sigma_{uc}|, \sigma_2/|\sigma_{uc}|)$ (Figure 31). The failure stresses are normalized by the uniaxial compressive strength σ_{uc}.The failure points present an increasing nonlinear evolution with an opening envelope translating thus the previous observations.

This behaviour can be interpreted from the increase of the contact surfaces between the crystals in compression and thus the resulting cohesion from friction. More, the biaxial compression generated in this type of tests leads to blocking or compressing the transversal strain (ε_{T1}), which prevents the propagation of the damage, thus increasing the apparent resistance by confinement effect.

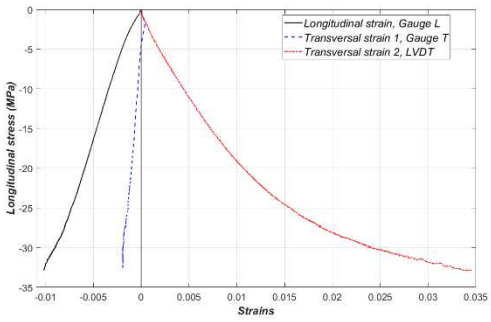

Figure 30. Evolution of the longitudinal stress in function of the strains in channel die test with $\sigma_T/\sigma_L = 0.5$

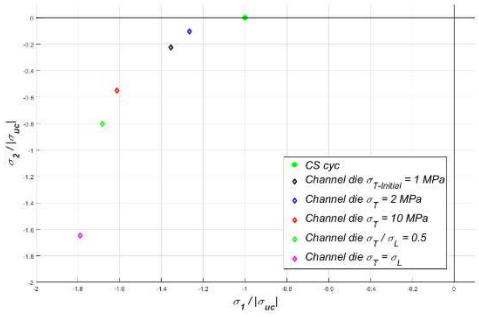

Figure 31. Failure stresses plotted in the stress plane

Table 2. Ultimate stresses and strains at break for channel die tests

Channel-die	$\boldsymbol{\sigma_L}$ **(MPa)**	$\boldsymbol{\sigma_{T1}}$ **(MPa)**	$\boldsymbol{\sigma_{T2}}$ **(MPa)**	$\boldsymbol{\varepsilon_L}$ **(%)**	$\boldsymbol{\varepsilon_{T1}}$ **(%)**	$\boldsymbol{\varepsilon_{T2}}$ **(%)**
$\boldsymbol{\sigma_{T-initial}}$ **= 1 MPa**	-26.47	-4.42	0	-1.072	0.537	3.792
$\boldsymbol{\sigma_T}$ **= 2 MPa**	-24.76	-2.054	0	-1.416	0.561	2.283
$\boldsymbol{\sigma_T}$ **= 10 MPa**	-31.51	-10.8	0	-0.679	-0.063	2.739
$\boldsymbol{\sigma_T/\sigma_L}$**= 0.5**	-32.88	-15.67	0	-1.021	-0.196	3.453
$\boldsymbol{\sigma_T = \sigma_L}$	-34.98	-32.2	0	-0.564	-0.418	3.838

3.8 Irreversible strains

Unloading steps followed by recovery steps highlight the presence of irreversible strains of plasticity or inter-granular friction type. The curves in Figure 32 show the evolution of the relaxed Von Mises stress as a function of irreversible longitudinal and transversal strains, for tension, compression and triaxial compression tests. In tension, irreversible strains are very low, and the behaviour is mainly viscoelastic. In compression, the levels of irreversible strains are higher: as mentioned above, in compression, the contact surface between crystals becomes important and a shear is developed in the microstructure of the material. This phenomenon is even more pronounced in triaxial compression where the material is consolidated under hydrostatic pressure.

It is difficult to find, at the same time, an internal variable of irreversible strain and an equivalent stress that could, by means of plasticity law, describe all tests with the same hardening curve.

In Figure 33, the relaxed Von Mises stress is plotted in function of the deviatoric plastic strain $\dot{\varepsilon}^p_{Dev} = \sqrt{\frac{2}{3}\dot{\varepsilon}^p_{Dev} : \dot{\varepsilon}^p_{Dev}}$. The differences between the curves suggest that the deviatoric

strain can't be linked to the same level of Von Mises stress for the different tests.

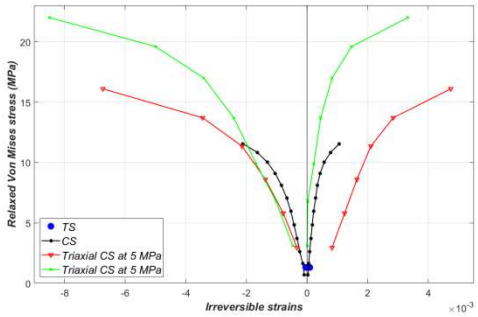

Figure 32. Evolution of relaxed Von Mises stress in function of irreversible strains in tension, compression and triaxial compression at 5 and 10 MPa

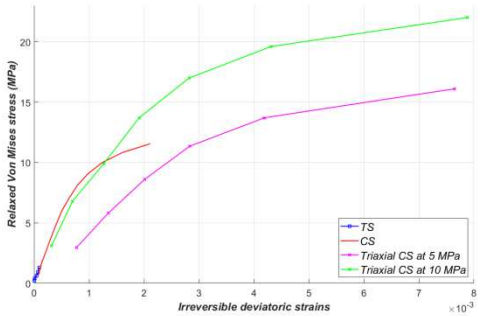

Figure 33. Evolution of relaxed Von Mises stress in function of deviatoric irreversible strains in tension, compression and triaxial compression at 5 and 10 MPa

An eventual consolidation effect is inspected. For this, the deviatoric irreversible strain is plotted in function of the deviatoric stress increased by the triaxial pressure weighted by a consolidation term c, $\sigma^{Mises} + c.\frac{1}{3}Tr(\sigma)$ in Figure 34. The curves are dispersed, and one consolidation parameter is not enough to obtain a representative model for the conducted tests, especially for low stress levels.

A concept of an effective quantity in plasticity could also be explored with a view to establish a hardening law.

Figure 35 shows the evolution of the irreversible volumetric strain $\varepsilon_{Vol}^{p} = Tr(\varepsilon^{p})$ in function of the deviatoric strain ε_{Dev}^{p}. It's noticed first that the level of the volumetric strain remains low compared to the deviatoric strain. The triaxial compression at 10 MPa presents the highest irreversible volumetric strain. Tension presents a dilatant behaviour from the beginning and stays very low. In compression, the behaviour becomes quasi deviatoric. When a hydrostatic pressure of 5 MPa is applied, the material seems highly dilatant from the beginning of the test. This observation is not expected for this test and probably coming from the high transversal strain observed at 5 MPa of hydrostatic pressure.

The channel die test with ratio 0.5, being monotonous, doesn't allow reporting points associated to the dilatancy. However, the 3 strains, in Figure 30, show an important positive volumetric strain, same as in triaxial compression at 5 MPa. It seems that the hydrostatic pressure consolidates, in terms of stress and stiffness, without generating negative volumetric flow as seen in triaxial compression at 10 MPa.

In the latter test, triaxial compression at 10 MPa, the presence of an important initial porosities allows a first step of contraction depending on the reached pressure level. It seems

that the material presents different physical phenomena in test with low level of confinement at high level of confinement. This response is difficult to interpret but suggests the need to do additional tests at intermediate hydrostatic pressure levels and arouses the question of the flow limit under only spherical confinement that exceeds 10 MPa.

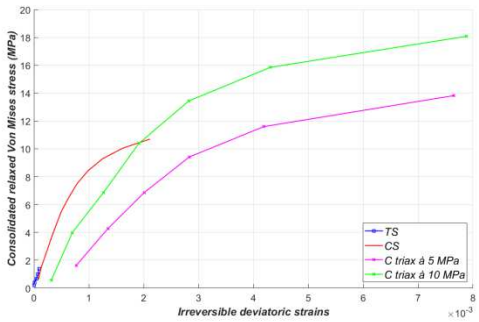

Figure 34. Evolution of consolidated relaxed Von Mises stress in function of irreversible strains in tension, compression and triaxial compression at 5 and 10 MPa

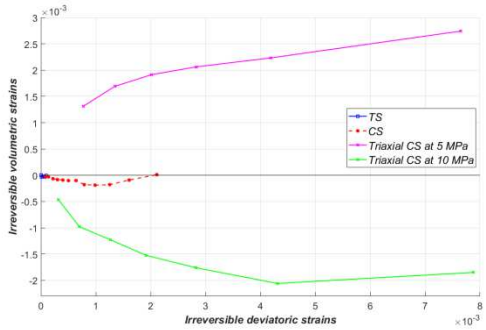

Figure 35. Evolution of irreversible volumetric strains in function of deviatoric irreversible strains in tension, compression and triaxial compression at 5 and 10 MPa

4. Modelling of the damage induced anisotropy and effectivity functions

4.1 Microplane model for Plastic-bonded explosives

This approach states that each direction of the solid angle characterizes a microplane on which the strain is decomposed. It should be noted that Microplane approach is not a micro-macro homogenisation model but rather a spatial partition. Constitutive equations are defined in the microplane level where the existence of free energy is assumed. The global stress tensor is determined by angular integration of the microplane stress vector over the whole solid angle. The global free energy Ψ^{glo} is equal to the angular integral over the entire solid angle Ω of the angular free energy density, expressed as $\Psi^i/4\pi$ and associated to each plane defined by its normal vector $\underline{n}^i$:

$$\psi^{glo} = \frac{3}{4\pi}\int_{\Omega}\psi^i(\underline{t}_\varepsilon, q)d\Omega, \quad \text{(Eq. 1)}$$

where the subscript i denotes the microplane orientation, $\underline{t}_\varepsilon = \underline{\underline{\varepsilon}}.\underline{n}^i$ represents a deformation vector and q is a set of state variables. The global stress tensor $\underline{\underline{\sigma}}$ is defined by the partial derivative of the free energy Ψ^{glo} with respect to the strain tensor $\underline{\underline{\varepsilon}}$:

$$\underline{\underline{\sigma}} = \frac{\partial \rho_0 \psi^{glo}}{\partial \underline{\underline{\varepsilon}}} = \frac{3}{4\pi} \int_\Omega \frac{\partial \rho_0 \psi^{i}(\underline{t}_\varepsilon, q)}{\partial \underline{\underline{\varepsilon}}} d\Omega \quad \text{(Eq. 2)}$$

It should be noted that variables underlined with one line are vectors, those underlined with two lines are twice rank tensors and those underlined with four lines are fourth rank tensors.

Many different Microplane formulations exist in the literature, based on the strain decomposition (Normal-shear, volumetric-deviatoric, etc.). Carol et al. (Carol, et al., 2001) proposed a thermodynamically consistent Microplane model with a Volumetric-Deviatoric-Tangential (V-D-T) split, i.e., with a decomposition of the strain tensor to volumetric, deviatoric and tangential components respectively noted ε_V, ε_D and $\underline{\varepsilon}_T$ and expressed as follows in each microplane:

$$\varepsilon_V = \frac{1}{3} \underline{\underline{1}} : \underline{\underline{\varepsilon}} = \underline{\underline{V}} : \underline{\underline{\varepsilon}} \quad \text{(Eq. 3)}$$

$$\varepsilon_D = \left(\underline{n} \otimes \underline{n} - \frac{1}{3} \underline{\underline{1}} \right) : \underline{\underline{\varepsilon}} = \underline{\underline{D}} : \underline{\underline{\varepsilon}} \quad \text{(Eq. 4)}$$

$$\underline{\varepsilon}_T = \left(\underline{n} \cdot \underline{\underline{I}} - \underline{n} \otimes \underline{n} \otimes \underline{n} \right) : \underline{\underline{\varepsilon}} = \underline{\underline{T}} : \underline{\underline{\varepsilon}} \quad \text{(Eq. 5)}$$

Equations (3), (4) and (5) define the projection of the global strain tensor on a microplane. It should be noted that ε_V is isotropic in the material. These strains allow the determination of stresses in a microplane with the following state laws:

$$\sigma_V = \frac{\partial \rho_0 \psi^{i}(\underline{t}_\varepsilon, q)}{\partial \varepsilon_V} \quad \text{(Eq. 6)}$$

$$\sigma_D = \frac{\partial \rho_0 \psi^{i}(\underline{t}_\varepsilon, q)}{\partial \varepsilon_D} \quad \text{(Eq. 7)}$$

$$\underline{\sigma}_T = \frac{\partial \rho_0 \psi^{i}(\underline{t}_\varepsilon, q)}{\partial \underline{\varepsilon}_T} \quad \text{(Eq. 8)}$$

The global stress tensor is then evaluated from the stresses defined in the microplanes by an integral over the solid angle Ω, using the following equation:

$$\underline{\underline{\sigma}} = \frac{3}{4\pi}\int_{\Omega}\left\{\sigma_V.\underline{\underline{V}} + \sigma_D.\underline{\underline{D}} + \underline{\sigma}_T.\underline{\underline{T}}\right\} \quad \text{(Eq. 9)}$$

When the Microplane approach is used to model only damageable elasticity, a global potential can be expressed by integration by taking into account a damaged elastic global anisotropic operator. Microplane approach can be used in this case only to define this operator without introducing all the variables at the level of microplanes. To model the induced anisotropic damage of the material, the free energy is defined as follows (Picart, et al., 2014):

$$\psi^i = \frac{1}{2}E_V\left(1-\alpha_V\left(\varepsilon_V\right)d_V\right)\varepsilon_V^2 + \frac{1}{2}E_D\left(1-\alpha_D\left(\varepsilon_D\right)d_D\right)\varepsilon_D^2 + \frac{1}{2}E_T\left(1-d_T\right)\underline{\varepsilon}_T.\underline{\varepsilon}_T \quad \text{(Eq. 10)}$$

In this equation, three damage variables d_V, d_D and d_T that affect the corresponding elastic moduli denoted, respectively, E_V, E_D and E_T, are introduced. These moduli are related to the bulk and shear global parameters K and μ as follows: $EV = 3K$ and $2ED + 3ET = 10\mu$ (Carol, et al., 2001). The damage is calculated at the level of microplanes. d_V is the same for all microplanes since ε_V is isotropic. d_D and d_T are calculated individually for each microplane, based on ε_D and $\underline{\varepsilon}_T$.

α_V and α_D are the effectivity functions defined, respectively, in terms of volumetric strain and deviatoric strain for each microplane. These effectivity functions manage the opening/closure of microcracks, asymmetry of the behaviour between tension and compression and the effect of hydrostatic pressure. It has been assumed that d_T is not affected by the effectivity. To avoid a spurious dissipation and discontinuity in the model responses and to obtain simple constitutive laws, α_V and α_D depend on their associated strain components. In the proposed model, the damage depends on the total strain. Volumetric and deviatoric damages are supposed effective when volumetric strain and deviatoric strain are positive, respectively. In the opposite case, the volumetric strain is supposed deactivated. For the deviatoric strain, a partial recovery of the deviatoric model is considered with $\alpha_D(\varepsilon_D) = 0.5$.

The assumed relationships between damage variables and their associated forces F_V, F_D and F_T are given in terms of ε_V, ε_D and $\underline{\varepsilon}_T$ respectively for each microplane:

$$F_V = -\frac{\partial \rho_0 \psi^i}{\partial d_V} = \frac{1}{2} E_V \alpha_V \left(\varepsilon_V\right) \varepsilon_V^2$$

(Eq. 11) $$F_D = -\frac{\partial \rho_0 \psi^i}{\partial d_D} = \frac{1}{2} E_D \alpha_D \left(\varepsilon_D\right) \varepsilon_D^2$$

(Eq. 12) $$F_T = -\frac{\partial \rho_0 \psi^i}{\partial d_T} = \frac{1}{2} E_T \underline{\varepsilon}_T . \underline{\varepsilon}_T$$

(Eq. 13)

Considering the effect of the pressure on the damage evolution and the dependency of this damage on strain, the following phenomenological relations have been proposed by (Picart, et al., 2014) in a microplane:

$$d_{V,D,T}\left(F_{V,D,T}, p\right) = \max\left(d^0_{V,D,T}, 1 - \exp\left[-p\left(a_1 F_{V,D,T}\right)^{a_2}\right]\right)_t, \; 0 \le d_{V,D,T} \le 1 \qquad \text{(Eq. 14)}$$

where:

$$p = 1 + \left[a_3 . H(-\varepsilon_V) + a_4 . H(\varepsilon_V)\right] E_V \left\langle \varepsilon_V - \varepsilon_V^{0-H10} \right\rangle_+ \qquad \text{(Eq. 15)}$$

The effectivity functions are defined as follows:

$$\begin{cases} \varepsilon_V \ge 0 \rightarrow \alpha_V\left(\varepsilon_V\right) = 1 \\ \varepsilon_V < 0 \rightarrow \alpha_V\left(\varepsilon_V\right) = 0 \end{cases} \qquad \begin{cases} \varepsilon_D \ge 0 \rightarrow \alpha_D\left(\varepsilon_D\right) = 1 \\ \varepsilon_D < 0 \rightarrow \alpha_D\left(\varepsilon_D\right) = 0.5 \end{cases} \qquad \text{(Eq. 16)}$$

In the previous equations, d^0_{VDT} is the initial damage in the material. The material parameters a_1 and a_2 manage the evolution of the damage versus the strain, and a_3 and a_4 manage the dependency of the damage on the pressure. The pressure dependency is carried out through the function p given by Eq. 14, where ε_V^{0-H10} is a third of the negative volumetric strain reached after hydrostatic compaction of 10 MPa. Thus, $p = 1$ in the beginning of the compression phase in the triaxial compression at 10 MPa ($\varepsilon_V = \varepsilon_V^{0-H10}$) and $p \gg 1$ in the beginning of the uniaxial compression.

Two damage evolution laws were integrated to manage the asymmetry between tension and compression based on ε_V in Eq. 15. The figure below shows the effect of the parameters on the damage evolution.

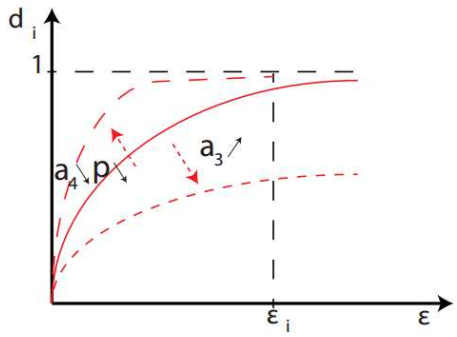

Figure 36. Damage evolution law (Benelfellah, et al., 2014)

The main limit of the models based on an additivity of oriented damages comes from the impossibility to experimentally identify the effect of each oriented microcracks group on the global mechanical response of the material. Thus, the parameters related to the damage evolution should be calibrated by comparing the numerical predictions of the material global behaviour to the test data.

4.2 New damage evolution laws and effectivity functions

4.2.1 Pre-damage

The pre-damage defined above allows the stiffness in tension to be properly adjusted since the damage is effective from the beginning. For compression and triaxial compression, this does not seem sufficient. A stiffening effect is therefore introduced into the model; the pressure acts both on the compressibility modulus K and on the shear modulus μ, but in two different ways.

4.2.2 Nonlinear volumetric elasticity

For the compressibility modulus K, the stiffening is considered as a non-linear function of the volumetric strain with a stiffening coefficient r_K as shown below. This parameter allows to describe the observed stiffening at the end of the pressurization cycles in triaxial compression tests. Heaviside-type effectivity functions alone can't describe this evolution. Thus, the compressibility modulus is defined as follows:

$K_{ref} = \frac{E}{3(1-2\upsilon)}$ (Eq. 17)

If $\varepsilon_V \leq 0 : K = \frac{K_{ref}}{(1+r_K \varepsilon_V)^2}$ with ($\varepsilon_V < 0$ in compression)

(Eq. 18)

– If not : $K = K_{ref}$

with υ is Poisson's ratio.

4.2.3 Elastic parameters

It has been observed that the modulus of the materials varies approximatively between around 1000 MPa in the beginning of uniaxial compression to 3000 MPa in the beginning of triaxial compression at 10 MPa of hydrostatic pressure. The Young's modulus of the material, considered not damaged, will be taken as observed in the beginning of the triaxial compression. An important level of pre-damage allows then, via an effectivity parameter, to find the initial modulus (lower) in uniaxial compression. The effectivity which allows this stiffness recovery is related to the shear moduli and is a function of the volumetric strain.

4.2.4 Damage evolution laws

Damage evolution laws are driven by the total deformation (and not the elastic deformation). In fact, the material response under triaxial compression presents a stress plateau during which the product of the elastic deformation by the Young's modulus is constant ($\varepsilon^e E$), which will lead to blocking the damage if it has been driven by ε^e, not observed experimentally.

To adjust the evolution of the damage, the two parameters a_1 and a_2 of Eq. 14 must be identified. These two parameters are chosen identical in Benelfellah's model for the three damage variables, even if the model gives us the possibility of having different parameters for d_V, d_D and d_T, and therefore to adjust their evolutions separately. It is assumed in the model that the three damage variables do not evolve in the same way. In tension, the normal to the failure surface is oriented according to the direction of the load. This suggests that it's the deviatoric damage d_D that predominantly develops there. In addition, we observed experimentally that the damage evolves as a function of the positive deformation, therefore as a function of the longitudinal deformation in tension, and transverse in compression. This encourages us to define the force that drives the deviatoric damage with a positive part, replacing Eq. 12:

$$F_D = \frac{1}{2}\alpha_D E_D \langle \varepsilon_D \rangle_+^2 \quad \text{(Eq. 19)}$$

In compression, it is rather the tangential damage d_T which is predominant since the failure is manifested according to the 45° failure surface. For the tangential strain, there is no

effectiveness in Benelfellah's model. Also, the force which drives the evolution of tangential damage is defined as a replacement for Eq. 13:

$$F_T = \frac{1}{2}\alpha_T E_T \boldsymbol{\varepsilon}_T . \boldsymbol{\varepsilon}_T \quad \text{(Eq. 20)}$$

The volumetric pre-damage is conserved. The force driving the volumetric damage is defined same as in Eq. 11. The damage evolution laws contain a function p defined as a function of the positive part and the negative part of the volumetric deformation, which reflects the effect of pressure on the evolution rate of damage. This function slows down (resp. accelerates) the evolution of damage under the effect of negative volumetric strain (resp. positive volumetric strain). This is redundant with the effectivity functions that deactivate (resp. activate) the effect of the damage according to the sign of the volumetric deformation. In our model, it's supposed that the effectivity with manage this effect in compression and only on the case of positive volumetric deformation, the damage evolution is accelerated by p. We therefore suggest defining the pressure the pressure function p only as a function of the positive volumetric deformation, replacing Eq. 15 as follows:

$$p = 1 + a_3 E_V \langle \varepsilon_V \rangle_+ \quad \text{(Eq. 21)}$$

Considering the mentioned observations above, three damage evolution laws are defined, for the three different damage variables for each microplane, replacing Eq. 14:

$$d_{V,D,T}\left(F_{V,D,T}, p\right) = max\left(d^0_{V,D,T}, 1 - exp\left[-p\left(a_{1V,D,T} F_{V,D,T}\right)^{a_2}\right]\right)_t \quad \text{(Eq. 22)}$$

with $0 \leq d_V, d_D, d_T \leq 1$.

4.2.5 Effectivity functions

To have a thermodynamically consistent model, the effectivity functions α_V, α_D and α_T must be defined in functions of their respective deformations ε_V, ε_D and ε_T. This does not seem sufficient to model the stiffening of the behaviour in function of the pressure and the nonlinearity in unloading steps. We will, thus, propose an effectivity function defined exclusively in function of the volumetric deformation ε_V. For the relatively proportional loading paths, it seems that the thermodynamics is relatively respected. During simulations, an energy balance will allow to assess this assumption. The effectivity functions initially defined, are based on Heaviside functions. The sudden variation of such a function does not correspond to what we want to describe, namely a gradual recovery of rigidity. We state that the damage is gradually deactivated by passing from a positive volume strain to a negative

volume strain. A tabulated law was thus proposed and defined between the responses of compression and triaxial compression at 5 MPa and a function between the triaxial compressions at 5 MPa and at 10 MPa. The damage is supposed to be completely deactivated, i.e., $\alpha_T = 0$, for a volumetric strain value, ε_V^{0-H10} to which it is considered that all the microcracks are closed. Nevertheless, there exist two different cases of loading with negative volumetric strain, compression and triaxial compression at two levels of pressure. The evolution of the effectivity function cannot be the same for a uniaxial test and a triaxial test. Figure 37 shows the change in tangential effectivity as a function of the volume deformation.

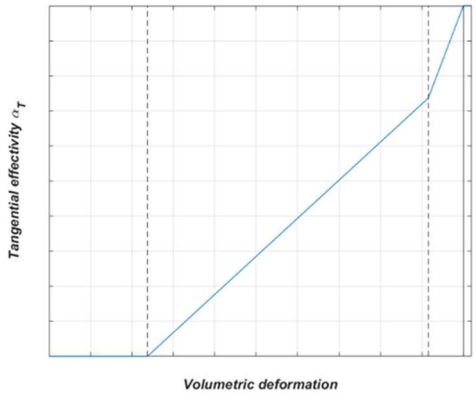

Figure 37. Evolution of the tangential effectivity in function of the volumetric deformation

The equations below define the function of tangential effectivity : he model:

- If $\varepsilon_V \geq 0$, $\alpha_T = 1$
- If $0 \geq \varepsilon_V \geq \varepsilon_V^{0-H5}$: $\alpha_T = 1 - \frac{1}{\beta \varepsilon_V^{0-H10}} \varepsilon_V$

If $\varepsilon_V^{0-H5} \geq \varepsilon_V \geq \varepsilon_V^{0-H10} : \alpha_T = \delta_a \varepsilon_V + \delta_b$ (Eq. 23)

With $\delta_a = \frac{1 - \frac{1}{\beta \varepsilon_V^{0-H10}} \varepsilon_V^{0-H5}}{\varepsilon_V^{0-H5} - \varepsilon_V^{0-H10}}$ (Eq. 24)

with $\delta_b = -\delta_a \varepsilon_V^{0-H10}$ and β is a parameter to identify.

ε_V^{0-H10} is the volumetric deformation at which the damage is no longer effective, i.e, $\alpha_T(\varepsilon_V^{0-H10}) = 0$. ε_V^{0-H5} is the volumetric deformation that defines the slope change of the tangential effectivity function.

Due to the complexity of the identification, we will simplify the model here by assuming that the deviatoric effectiveness evolves in the same way as the tangential effectiveness:

$$\alpha_D = \alpha_T \quad \text{(Eq. 25)}$$

The difficulty of such model is the calibration. The parameters of the model drive the rate of evolution of the damage and the effectivity that evolve progressively at the same time. The combination of these two physical phenomena should give the desired material behaviour and especially the desired damaged modulus evolution.

The calibration and the simulations of all the tests will be detailed in future works.

This research work gave many interesting perspectives. Two major points will be discussed in the future works. Two additional non-proportional tests, 0°-90° compression, torsion and confined torsion will give an additional insight on the material behaviour. The 0°-90° compression test will give an additional light as to the longitudinal stiffness associated with the transverse direction. This information isn't available in all the previous tests. The torsion and confined torsion tests will allow the analysis of the damage and the effectivity in different planes under positive and negative strains evolving at the same time.

Also, an anisotropic viscoelastic-plastic model is needed to model the studied behaviour. The material presents an important viscous component that should be taken into account in an anisotropic framework. Also, the evolution of irreversible strains seems complex and could be modelled using multiple load surfaces defined in the different microplanes.

5. Conclusion

An original experimental study of a simulant material for Plastic-Bonded explosives composed of uniaxial, cyclic, alternated, and non-proportional tests was presented in this article.

Microstructural observations show an initial pre-damage in the pristine material generated by the manufacturing process. The microstructure is initially considered isotropic in the sense that it doesn't have a preferred microcracks orientation. These microcracks evolve randomly under loading with different failure mechanisms. In tension, binder-crystals debonding is observed with inter-granular cracks. Granular cracks and fracture crystals are still present but rarely observed. Compression presents a more violent damage with fractured crystals and shear bands.

These different phenomena yield a complex macroscopic behaviour. The opening/closing of microcracks in tension/compression under the longitudinal strains induces an asymmetry of behaviour. In tension, the behaviour is brittle, and the damage evolves rapidly unlike

compression where the material shows a stiffening behaviour at the beginning and then softening. The alternated tests highlight the presence of damage effectivity which plays a role of the same order or even predominant, in the evolution of stiffness in terms of degradation, and in recovery.

Under biaxial compression, higher strengths than in uniaxial compression were shown. In the triaxial compression, the sensitivity of the material to pressure was observed. The confinement of the material increases its rigidity, as well as the stress and the strain at break.

Regarding the sensitivity of the behaviour to the strain rate, the cyclic tests with relaxation and recovery steps and the DMA tests show a viscoelasticity which can be considered linear and independent of the pressure.

Finally, the evolution of irreversible deformations in the various tests was underlined. Its evolution seems complex. A single load surface controlling the evolution of the load surface using simplifying assumptions seems a strong hypothesis. A complex dilating nature has been observed also.

This experimental investigation highlighted the complexity of the damage evolution and effectivity phenomena in the material. The existing models are simplistic and enable to model the evolution of the damaged stiffness of the material. The proposed evolution stipulated a directional damage following microplanes orientation with volumetric, deviatoric and tangential components. Volumetric effectivity is defined with Heaviside functions while the deviatoric and tangential effectivity functions are a linear function with two different slopes based on the level of hydrostatic pressure ensuring thus a progressive closure of microcracks in function of the negative volumetric deformation.

This experimental investigation will be used to develop and identify a constitutive material model taking into account damage induced anisotropy, effectivity, viscoelasticity and plasticity. The proposed model will be completed with viscoelasticity (as in (Chatti, et al., 2019)) and plasticity embedded in the microplanes. The available experimental data will be used to calibrate the material parameters and then simulate the cyclic uniaxial, multiaxial, proportional, and non-proportional tests.

Acknowledgements**.** Authors thank "la Région Centre Val de Loire, France" and "INSA Centre Val de Loire" for funding this project.

References

Bailly, P. et al., 2011. Dynamic behavior of an aggregate material at simultaneous high pressure and strain rate: SHPB triaxial tests. *International journal of impact engineering,* Volume 38, pp. 73-84.

Bailly, P. et al., 2011. Dynamic behavior of an aggregate material at simultaneous high pressure and strain rate: SHPB triaxial tests. *International journal of impact engineering,* Volume 38, pp. 73-84.

Bargellini, R., Halm, D. & Dragon, A., 2007. Discrete approach for modelling quasi-brittle damage : conditions on the set of directions. *Comptes Rendus Mécanique,* 335(12), pp. 781-786.

Bargellini, R., Halm, D. & Dragon, A., 2008. Modelling of quasi-brittle behaviour: a discrete approach coupling anisotropic damage growth and frictional sliding. *European Journal of Mechanics,* 27(4), pp. 564-581.

Bazant, Z. P. & Gambarova, P. G., 1984. Crack shear in concrete: Crack band microplane model. *Journal of structural engineering,* Volume 110, pp. 2015-2035.

Belmas, R., 1994. *Mechanical behaviour of passed explosives.* Orlando, USA, International Symposium of Engineering Material Technology.

Benelfellah, A., 2013. *Contribution à la modélisation de l'anisotropie induite par endommagement d'un materiau aggrégataire energétique.* Tours: Université François Rabelais de Tours.

Benelfellah, A. et al., 2014. Analytical and numerical comparison of discrete damage models with induced anisotropy. *Engineering Fracture Mechanics,* Volume 121-122, pp. 28-39.

Bennett, J. G. et al., 1998. A constitutive model for the non shock ignition and mechanical response of high explosives. *Journal of the Mechanics and Physics of Solids,* 46(12), pp. 2303-2322.

Burlion, N., 2010. Test techniques and experimental characterization. Dans: J. Torrenti, G. Pijaudier-Cabot & J. Reynouard, éds. *Mechanical behavior of concrete.* s.l.:ISTE, WILEY.

Caliez, M. et al., 2014. Viscoelastic plastic model and experimental validation for a granular energetic material. *International journal of energetic materials and chemical propulsion,* 13(4), pp. 339-371.

Carol, I., Jiràsek, M. & Bazant, Z. P., 2001. A thermodynamically consistent approach to microplane theory. Part I. Free energy and consistent microplane stresses. *International Journal of Solids and Structures,* 38(17), pp. 2921-2931.

Chatti, M. et al., 2019. Modelling of the viscoelastic behaviour with damage induced anisotropy of a plastic-bonded explosive based on the microplane aproach. *International Journal of Solids and Structures,* Volume 168, pp. 13-25.

Dienes, J. K., 1982. *Permeability, percolation and statistical crack mechanics.* Berkeley, California, American Rock Mechanics Association.

Dienes, J. K., 1996. A unified theory of flow, hot spots, and fragmentation with an application to explosive sensitivity. Dans: *High-Pressure Shock Compression of Solids II.* New York: L. Davison et al., eds., Springer, p. 366–398.

Dienes, J. K., Zuo, Q. H. & Kershner, J. D., 2006. Impact initiation of explosives and propellants via statistical crack mechanics. *Journal of the Mechanics and Physics of Solids,* 54(6), pp. 1237-1275.

Ellis, K., Leppard, C. & Radesk, H., 2005. Mechanical properties and damage evolution of a UK PBX. *Journal of materials science, 23,* pp. 6241-6248.

Gratton, M. et al., 2009. Mechanical characterization of a viscoplastic material sensitive to hydrostatic pressure. *European Journal of Mechanics - A/Solids,* 28(5), pp. 935-947.

Hackett, R. M. & Bennett, J. G., 2000. An implicit finite element material model for energetic particulate composite materials. *International Journal for Numerical Methods in Engineering,* Volume 49, pp. 1191-1209.

Idar, D. J., Peterson, P. D., Scott, P. D. & Funk, D. J., 1998. Low strain rate compression measurements of PBXN-9, PBX9501 and Mock9501. *Shcok compression of condensed matter,* p. 587.

Le, V. D., 2007. *Modélisation et identification du comportement plastique visco-élastique endommageable d'un matériau agrégataire.* Tours: Université François Rabelais.

Le, V. D. et al., 2010. Experimental mechanical characterization of plastic-bonded explosives. *Journal of materials science,* Volume 45, pp. 5802-5813.

Liu, M. et al., 2020. Modeling of the deformation and damage of plastic-bonded explosive in consideration of pressure and strain rate effects. *International Journal of Impact Engineering,* Volume 146.

Liu, Z. W. et al., 2009. Fracture behavior of PBX simulant subject to combined thermal and mechanical loads. *Polymer testing,* 28(6), pp. 627-635.

Maire, J. F. & Chaboche, J. L., 1997. A new formulation of continuum damage mechancis (CDM) for composite materials. *Aerospace Science and Technology,* 1(4), pp. 247-257.

Murakami, S. & Kamiya, K., 1997. Constitutive and damage evolution equations of elastic-brittle materials based on irreversible thermodynamics. *International Journal of Mechanical sciences,* 39(4), pp. 473-486.

Parab, N. D. et al., 2016. High speed X-ray phase contrast imaging of energetic composites under dynamic compression. *Applied Physics Letters,* Volume 109.

Park, C., Jeong, S., Huh, H. & Park, J., 2013. Material Behaviors of PBX Simulant with Various Strain Rates. *Key Engineering Materials,* pp. 117-120.

Pecqueur, G., 1995. *Étude expérimentale et modélisation du comportement d'une craie et d'un grès en torsion.* Lille: Université de Lille 1.

Picart, D. et al., 2014. Characterization and modeling of the anisotropic damage of a high-explosive composition. *Engineering Fracture Mechanics,* Volume 131, p. 525–537.

Picart, D. et al., 2014. Characterization and modeling of the anisotropic damage of a high-explosive composition. *Engineering Fracture Mechanics,* Volume 131, p. 525–537.

Picart, D. & Brigolle, J. L., 2010. Characterization of the viscoelastic behaviour of a plastic bonded explosives. *Materials science and engineering: A,* Volume 527, pp. 7826-7831.

Picart, D., Damiani, D. & Doucet, M., 2012. *The reverse edge-on impact test; a small scale experiment for non-shock ignition studies.* s.l., AIP Conference Proceedings, American Institute of Physics , pp. 497-500.

Picart, D. & Pompon, C., 2016. Experimental characterization of the multiaxial failure of Plastic Bonded Explosive. *International Journal of Energetic Materials and Chemical Propulsion,* 15(2), pp. 141-165.

Plassart, G. et al., 2020. Quasistatic mechanical behavior of HMX- and TATB-based plastic-bonded explosives. *Mechanics of Materials,* Volume 150.

Ravindran, S., Tessema, A. & Kidane, A., 2016. Local Deformation and Failure Mechanisms of Polymer Bonded Energetic Materials Subjected to High Strain Rate Loading. Volume 2, p. 146–156.

Rja Fi Allah, S., 2006. *Modélisation du comportement mécanique d'un matériau agrégataire.* Tours: Université François Rabelais.

Trumel, H., Lambert, P. & Belmas, R., 2010. *Mesoscopic investigations of the deformation and initiation mechanisms of a hmx-based pressed composition.* Coeur d'Alene (ID), USA, s.n.

Wiegand, D. A., 2000. Mechanical failure of composite plastic bonded explosives and other energetic materials. *Proceedings of the 11 detonation symposium,* p. 744.

Williamson, D. M. et al., 2008. Temperature-time response of a polymer bonded explosive in compression (EDC37). *Journal of Physics D: Applied physics,* pp. 85404-85414.

Xiao, Y. et al., 2017. Characterization, modeling and simulation of the impact damage for polymer bonded explosives. *International Journal of Impact Engineering,* Volume 103, pp. 149-158.

Yeom, K. S., Jeong, S., Huh, H. & Park, J., 2012. New pseudo-elastic model for polymer-bonded explosive simulants considering the Mullins effect. *Journal of composite materials,* 47(27), pp. 3401-3411.

You, S., Chen, M.-W., Dlott, D.-D. & Suslick, K.-S., 2015. Ultrasonic hammer produces hot spots in solids. *Ultrasonic hammer produces hot spots in solids,* 6(6581).

Zhou, Z., Chen, P., Huang, F. & Liu, S., 2011. Experimental study on the micromechanical behavior of a PBX simulant using SEM and digital image correlation method. *Optics and Lasers in Engineering,* Volume 49, pp. 366-370.

Zhu, Q. Z., Shao, J. F. & Kondo, D., 2008. A micromechanics-based non-local anisotropic model for unilateral damage in brittle materials. *Comptes Rendus Mécanique,* 336(3), pp. 320-328.